

# Forecast for Epoch-of-Reionization as viewable by the Primeval Structure Telescope (PAST)

Ue-Li Pen<sup>1,2\*</sup>, Xiang-Ping Wu<sup>2</sup> and Jeff Peterson<sup>3</sup>

<sup>1</sup> Canadian Institute for Theoretical Astrophysics, 60 St. George St., Toronto, M5S  
3H8, Canada

<sup>2</sup> National Astronomical Observatories, Chinese Academy of Sciences, Beijing 100012,  
China

<sup>3</sup> Carnegie Mellon University Pittsburgh, USA

Received 2004 month day; accepted 2004 month day

**Abstract** We present sensitivity forecasts for the PAST 21cm reionization observations and compare these with the measured sensitivity of a prototype array. We discuss the likely epoch-of-reionization structures and the redshifts that can be observed, and conclude that a 10,000 antenna PAST will be able to image ionized structures with its 1 million pixel map at  $6 < z < 20$ . The angular scales of the images to be produced span from 5 arc minutes to 10 degrees. The effect of potential foreground contaminants are analyzed. All known extra-terrestrial foregrounds have power law continuum spectra, and can be modeled and cleanly separated. We present results of observations using the prototype, which verify the estimated sensitivities and provide data on astronomical foregrounds. The same sample allows real-world measurement of man-made interference, of meteor scatter propagation, and of ionospheric variation. These data are also used to verify our large angle map making algorithms.

**Key words:** cosmology: redshift survey, reionization

## 1 INTRODUCTION

The frontier of optical observation of the universe is traced by the furthest quasars ( $z \sim 6.41$ : White et al. (2003)) and galaxies (Pelló et al., 2004). Measurement of the

---

\* E-mail: pen@cita.utoronto.ca

absorption of UV light from quasars allows the late ionization history to be traced. This history has raised some apparent contradictions, which we will discuss below. Using VHF radio observations of line emission it may be possible to directly examine ionization at much higher redshifts— perhaps to redshift 20. With the Primeval Structure Telescope (PAST) it should be possible to directly study the Epoch of Reionization, mapping high redshift ionized structures in three dimensions.

A definitive measurement of the epoch of reionization (EOR) has many implications. It breaks some degeneracies in the CMB determinations of cosmological parameters by providing a direct measure of optical depth. By studying ionization one learns how the dark ages ended, and about the energetics of the first objects. In addition, such observations provide a very large number of resolved objects with direct redshift measurements. These can serve as source screens of beacons, allowing mapping of density concentrations in the high redshift universe using gravitational lensing (Pen, 2004).

## 1.1 History

We start with a brief review of the related cosmic history. After recombination at  $z = 1100$ , the universe enters a period popularly called the 'dark ages'. The CMB is a blackbody at  $T = 2.7(1+z)$ K with very little structure. The neutral baryonic component expands adiabatically with a kinetic temperature colder than the CMB by  $[(1+z)/1100]^{5/3}$ . The spin temperature of the 21cm transition is initially in thermal equilibrium with the CMB, and decoupled from the baryon kinetic temperature.

Around  $z \sim 100$ , the first non-linear objects form. The gas cannot cool radiatively, and acquires the same virial temperature as the dark matter, well above the CMB temperature. For the first such 'minihalos', the characteristic temperature is hundreds of degrees, at overdensities of several hundred. At such densities and temperature, the hydrogen nuclear spin temperature couples to the kinetic temperature of the gas (Madau et al., 1997). By redshift 20, a major fraction of matter is in virialized gravitationally bound halos, which, being warmer than the CMB, emit on the 21cm line. The minihalos are optically thin, and we see these clouds spread out in redshift. So, for observations that do not resolve the clouds, the 21 cm emission becomes an effective continuum, with slight intensity variations that track the average density. In this way the warm gas is observable via a brightness increment above the CMB. The typical surface brightness is 23 mK (Iliev et al., 2003).

The universe is ionized today, but the precise timing and history of reionization is not known. WMAP has measured the temperature polarization cross correlation, which constrains the reionization redshift  $9 < z_r < 20$ . This constraint appears robust, but at odds with quasar spectra which show the Gunn-Peterson effect indicating a late reionization  $z_r \sim 7$  (White et al., 2003; Wyithe & Loeb, 2004). CMB polariza-

tion arises from Thomson scattering of CMB photons off free electrons, which translates CMB quadrupole fluctuations into a polarization signal. Since the CMB fluctuation amplitude is known, the observed polarization directly maps into a Thomson optical depth  $\tau = 0.17 \pm 0.02$  (Kogut et al., 2003). One needs to add all electrons up to redshift  $z \sim 15$  to accumulate this optical depth.

Quasars from SDSS shows Ly $\alpha$  completely absorbed (White et al., 2003) at  $6 < z < 6.3$ . Using the also fully absorbed Ly $\beta$  line, they constrain the optical depth of  $\tau(\text{Ly}\alpha) > 22$ . For a neutral universe,  $\tau_{\text{GP}} = 3.42 \times 10^5 [(1+z)/7.08]^{3/2}$ . This translates into a neutral fraction greater than 0.006%. If both measurements are correct, the appearance of a neutral fraction above  $z=6$ , seen via quasars, and the large ionized fraction implied by WMAP, then either reionization proceeded very gradually or there was more than one reionization (White et al., 2003; Wyithe & Loeb, 2004). We discuss these possibilities below.

Reionization has two potentially observable effects on the 21cm brightness. It changes the global sky spectrum (Shaver et al., 1999), and also generates spatial structure (Furlanetto et al., 2004; Pen, 2004). With PAST we will search for spatial structure.

## 1.2 Cosmic Reionization Conundrum

If the source of ionizing radiation is stars or quasars, the transition must occur causally with localized sources. This presents a challenge: is it possible to ionize the universe homogeneously, and therefore gradually, through an opaque medium? Studies of quasar spectra constrain the Ly $\alpha$  optical depth, while it is the UV continuum optical depth that controls ionization. However, the equivalent width of the Ly $\alpha$  line is comparable to that in the continuum. For example, over the optically thick redshift range  $6.1 < z < 6.3$  observed by SDSS, the total equivalent width on Ly $\alpha$  is  $\tau(\text{Ly}\alpha)\Delta z/z \sim \tau_{\text{continuum}} > 1$ . This suggests that it is difficult for continuum photons to enter the dark regions in the quasar spectra. Only a region containing a continuum source can maintain a high ionization fraction. The ionizing sources are localized.

We think of re-ionization occurring through many Stromgren spheres, which grow and overlap. Each Stromgren sphere is a region of optically thin ionized material surrounding an ionizing source. UV continuum radiation propagates freely inside the sphere, but cannot penetrate the surrounding material. The transition from ionized and neutral is very sharp, unless the radiation is very hard. These Stromgren spheres grow with time. At some point, they start overlapping, which marks the completion of reionization. This completion has some resemblances to the nucleation of a first order phase transition. When these spheres overlap, the neutral fraction drops very suddenly. In a single Stromgren sphere, each ion sees just the radiation from its ionizing source. Once the spheres overlap, each atom sees all the ionizing sources all the way to the Hubble radius. Just as

in Olber's paradox, the brightness is now dominated by the far away sources. The flux increases as the ratio of the mean separation between ionizing spheres to the Hubble radius. This separation is most popularly modeled as the separation between the most massive minihalos, which is several comoving Megaparsecs. At any rate, the separation would have to be significantly smaller than the  $\Delta z = 0.2$  width of the SDSS absorption trough. The Hubble radius is two orders of magnitude larger, so the neutral fraction in the ionized regions should drop by two orders of magnitude at the end of the epoch of reionization, thereby reducing the optical depth on the continuum to less than 1%. At this point, the optical depth on the Ly $\alpha$  line should be significantly lower than unity, at quite apparent odds with the SDSS quasar data.

Other arguments based on the expansion speed of the Stromgren spheres around the known quasars at  $z > 6.1$  also suggest a mostly neutral IGM at these redshifts (Wyithe & Loeb, 2004).

We are faced with a paradox that the SDSS quasar spectra imply an ionization redshift close to 6, while WMAP implies larger than 10. There are a couple of possible resolutions from this paradox. One possibility is that the Stromgren spheres are comparable in size to the Hubble radius. Another is that reionization occurred twice (Cen, 2003). In such a scenario, the first reionization would occur at high redshift, say 20, possibly as a result of molecular hydrogen cooling. The ionizing sources turn off again, and the hydrogen recombines. It then reionizes again near redshift of 6, perhaps as a result of instabilities arising from atomic hydrogen line cooling. Other more exotic possibilities include ionization from hard X-ray or  $\gamma$  rays, which would generate fuzzy boundaries in the Stromgren spheres. Uniform radiation from a decaying dark energy or decaying dark matter would also not be subject to these constraints.

### 1.3 An Opportunity

Both theoretical analysis and the data indicate that the ionization history may have been very complex. A direct mapping of the neutral gas would provide the data to the re-ionization debate. Such data would help answer questions about the epochs of reionization, the physical scales of the process, and simply provide a new probe into the high redshift universe. In this paper we will outline the PAST strategy to achieve this goal. We note that the characteristic angular scales (5'-20'), surface brightness (23mK), flux level (0.1 mJy), and spectral resolution (300 khz) are all straightforward in modern day radio astronomy. Several existing arrays would have enough sensitivity to image reionization. The only obstacle is the serious man-made radio interference over the broad VHF band, which includes TV and FM radio.

In this paper we will address questions of sensitivity, foreground confusion, and data processing challenges. We will describe the prototyping campaign in section 2. In section

4 we describe the observing strategy to minimize the impact of foreground sources. The foregrounds have spatial but not frequency structure, while the ionization signals have both. We discuss below how to exploit this fact to achieve the required sensitivities. We have designed the PAST array to detect and map the ionization signals. PAST will use high gain phased arrays fixed pointed at the NCP.

## 2 PROTOTYPE AND SITE TEST

A series of site tests were performed over the period of August 2003-April 2004 at three sites in the XinJiang Autonomous Region, one site in Qinghai Province and at the South Pole. All sites were visited and tested for radio frequency interference (RFI). Each site has advantages, but at this stage of the project, accessibility is very important. We chose Ulaistai in western China, at  $90^\circ$  E,  $43^\circ$  N, and an altitude of 2600m for the current round of prototype testing. The site is surrounded by mountains over 4000m on all sides, which act as an excellent ground shield against RFI. The nearest cities are Korla and Urumuqi, each about 200 km away. The valley itself is served by a major railroad, and by roads that are open all year. The railroad uses a narrowband FM communication channel at 137.44 MHz. Electrical power mains provide AC power on-site. Cell phone towers serve the area, and service is good at the site, but the cell-nodes and handsets but do not interfere at the frequencies of interest.

### 2.1 Prototype Setup

The most extensive prototype testing was performed over the period March 1-5, 2004. Four phased arrays (called pods) of 7 log periodic antennae were set up on an approximate east-west baseline of 1.1km. Two pods were near the processing facility, and two more were connected by an intensity modulation analog fiber optic link. Logistic and technical support was provided by the Urumqi radio observatory.

We have built and tested several antenna designs, including a small loop antenna, a three octave log periodic dipole array, and a square log spiral antenna. For the test described here we used a two octave log periodic dipole array. The elements are horizontally polarized. The longest element length is 1m measured from the central transmission line to the edge, the self-similar parameter is  $\sigma = 0.26$  and  $\tau = 0.76$ . The number of elements (9) was chosen to allow high gain operations from 80-300 MHz. Numerical simulation of the design, placed over a ground plane, indicates about 10 dbi gain. Below 80 MHz the antenna has no resonant active region and behaves as a short dipole close to the ground. From 80 to 200 MHz the antenna matches the 50 ohm feedline with SWR below 2:1. At our lowest operating frequency, 50 MHz, the antenna presents impedance  $2 - j 200$  ohms, an inefficient match to the 50 ohm feedline. However we intend to use amplifiers with noise temperature below 40 K, and the sky brightness temperature at 50 MHz is

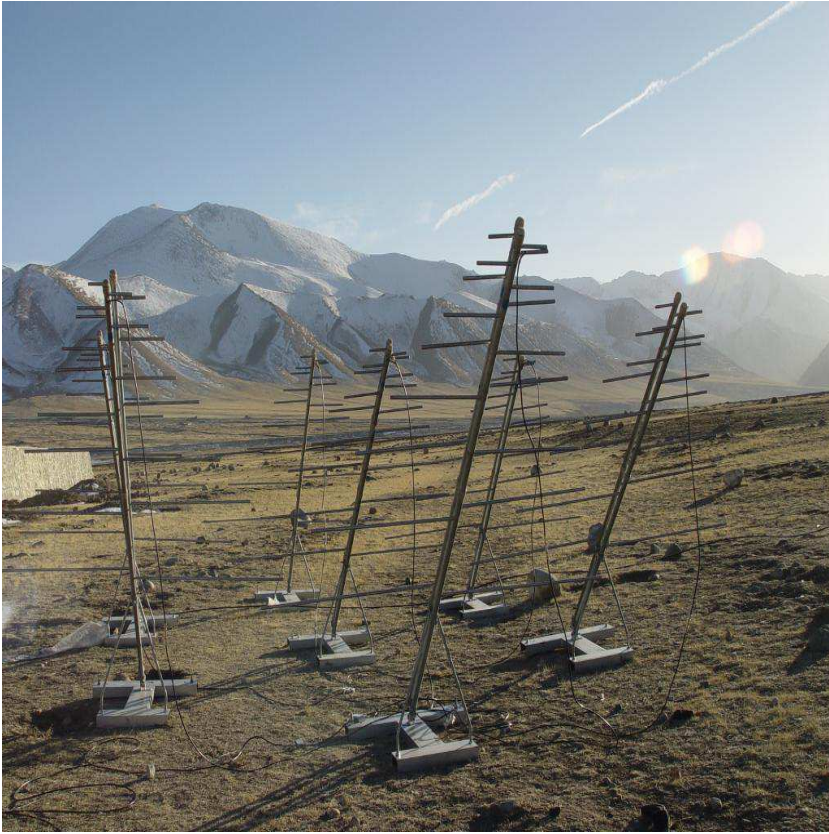


**Fig. 1** Prototype pod layout. The pod has an element separation between neighboring antennae of 2m when projected onto the NCP. The elements were summed with the appropriate delay lines to place the main lobe on the NCP.

about 4000 K so even with low coupling efficiency sky noise will exceed the amplifier noise contribution.

Each pod was a closed packed hexagon pointed at the north celestial pole (NCP). Figure 1 shows the layout. The projected separation was 2m for each side length. The phased array spacing is chosen to optimize performance near 100 MHz, with some compromise of performance at the extremes of the range. In the current layout the effective area of the individual antennas does not sum at low frequencies, and at high frequencies, array phasing sidelobes appear. For our next design we plan to increase the high frequency gain of the antenna to reduce the variation of effective area with frequency.

The elements were summed in phase using coaxial cable delay lines and commercial TV splitters, used in reverse as power combiners. The signal was bandpass filtered, amplified, and transmitted over the fiber link. The data were digitized using a commercial four channel 8-bit analog-digital converter board from Acquisition Logic, which was sited in a dual Xeon 2.4 GHz server PC.

During operations, the westernmost pod did not work properly, however 14 hours of data were obtained on the remaining three baselines. Observations started at 19:21 on March 3, 2004, Beijing time, and ended at 11:42 on March 4, 2004. The results obtained from the data are described in subsequent sections.

### 3 PROTOTYPE SENSITIVITY

Data from the prototype allows us to compare forecast sensitivity with sensitivity measure using sources on the sky. In the maps we have created, the two brightest sources within 10 degrees of the NCP are 3C061.1 at  $z=0.18$  and 3C390.3 at  $z=0.56$ . These we detect at 34 and 38 sigmas respectively. Their flux at 75 MHz, interpolated from the 6C survey at 151 MHz and the 8C at 38 MHz are 59 and 69.4 Jy. At 75 MHz the array has about 10.5 dBi gain. The effective area is then  $A_{\text{eff}} = G\lambda^2/(4\pi) = 14.1\text{m}^2$ . Using our effective bandwidth of  $\Delta\nu = 25$  MHz, this results in a net power of  $P_{3C061.1} = FA\Delta\nu/2 = -128.9$  dbm through each pod for 3C061. Slightly more uncertain is the noise of the system. The galaxy has a surface brightness on the pole of 1600K at 75 Mhz. This contributes a noise equivalent power  $P_{\text{noise}} = kT\Delta\nu = -95.3$  dBm. Our summing elements also had losses. On a network analyzer, each summing element had an insertion loss of 1.2 dB, and two summations were inserted. The amplifiers had estimated noise figures of 4 dB, and we budget an extra 3 dB for the remaining connector elements and impedance mismatches, for a total noise figure of 10dB. This corresponds to another 1500K from the amplifier noise, which doubles our effective noise budget. Our total signal to noise after 14 hours of integration is forecast to be  $\eta\sqrt{2t\Delta\nu}P_{3C061.1}/P_{\text{noise}} = 66$  where we used  $\eta = \sqrt{1/8}$  as the correlator efficiency, and the factor of 2 in the square root comes from the two correlation phases. Our digital sampling board had a net duty cycle of 1/4 due to the PCI bus transfer limitations, and the correlation software had not been optimized on the single PC. This estimate is close to the actual observed signal-to-noise. The measured and forecast sensitivity match to within the uncertainty due to loss of coherence due to the ionosphere, and unknown impedance mismatches.

### 4 FOREGROUND SEPARATION STRATEGY

The foregrounds exceed the reionization signal by at least a factor 1000. To remove them we will need to use both spatial and spectral discrimination. We list the foregrounds below along with our strategy for separation of the signal from the foreground.

#### 4.1 EMI

Since the band we will observe spans the FM broadcast, television broadcast and FM communications bands, man-made electromagnetic interference (EMI) can be severe at many sites. We minimize EMI by using earth curvature and mountain ranges.

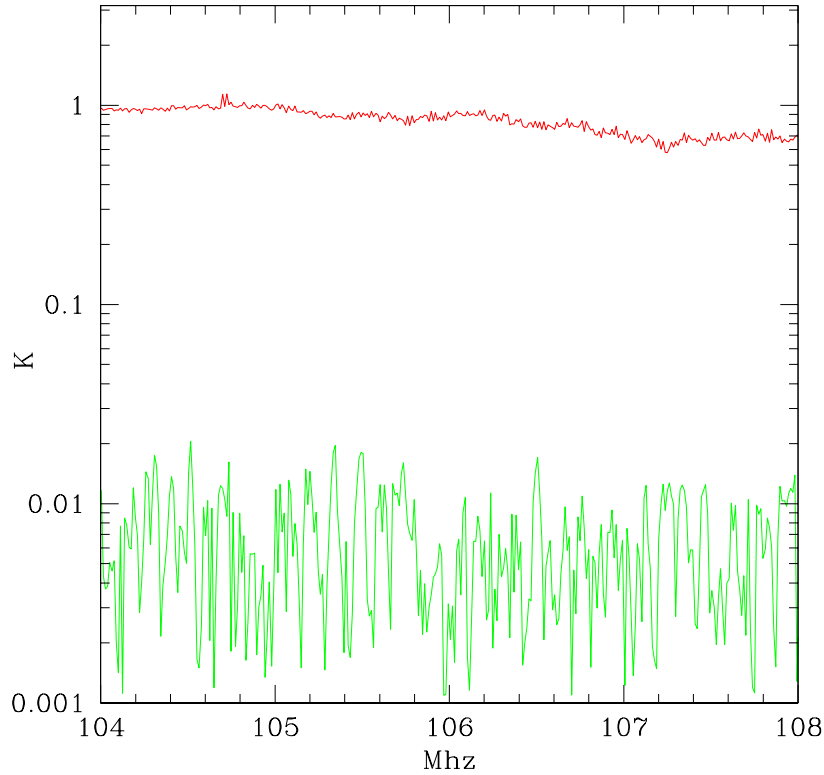


**Fig. 2** Spectrum taken at Ulastai on Jan 2, 2004. Shown is a short region in the FM band, which is usually the worst RFI regime. The upper line is the noise after a 30 second integration, while the lower line shows the spectrum after an 8 hour integration. Only the frequency range 104-108 was plotted to make the structures visible. High intensity meteorite peaks have been cut. We see that no sources of interference are visible with an antenna temperature greater than 20mK.

Figure 2 shows the sky spectrum taken during a site testing on Jan 2, 2004. The commercial FM 88-108 MHz band is often considered the worst for interference. We see no persistent sources down to 10 mK. The only detectable source are intermittent transmissions from the trains at 137 Mhz. Residual EMI can be filtered, or mitigated (Briggs et al., 2000), but so far it has been sufficient to simply ignore the line at 137 MHz.

When meteorites enter the upper atmosphere, they burn up and leave a trail of ionized plasma. The plasma frequency in this trail is significantly higher than the general ionosphere, and can reflect sources at ranges as far as 2200 km. In the test data, we can clearly see these meteor events. Figure 3 shows the effect.

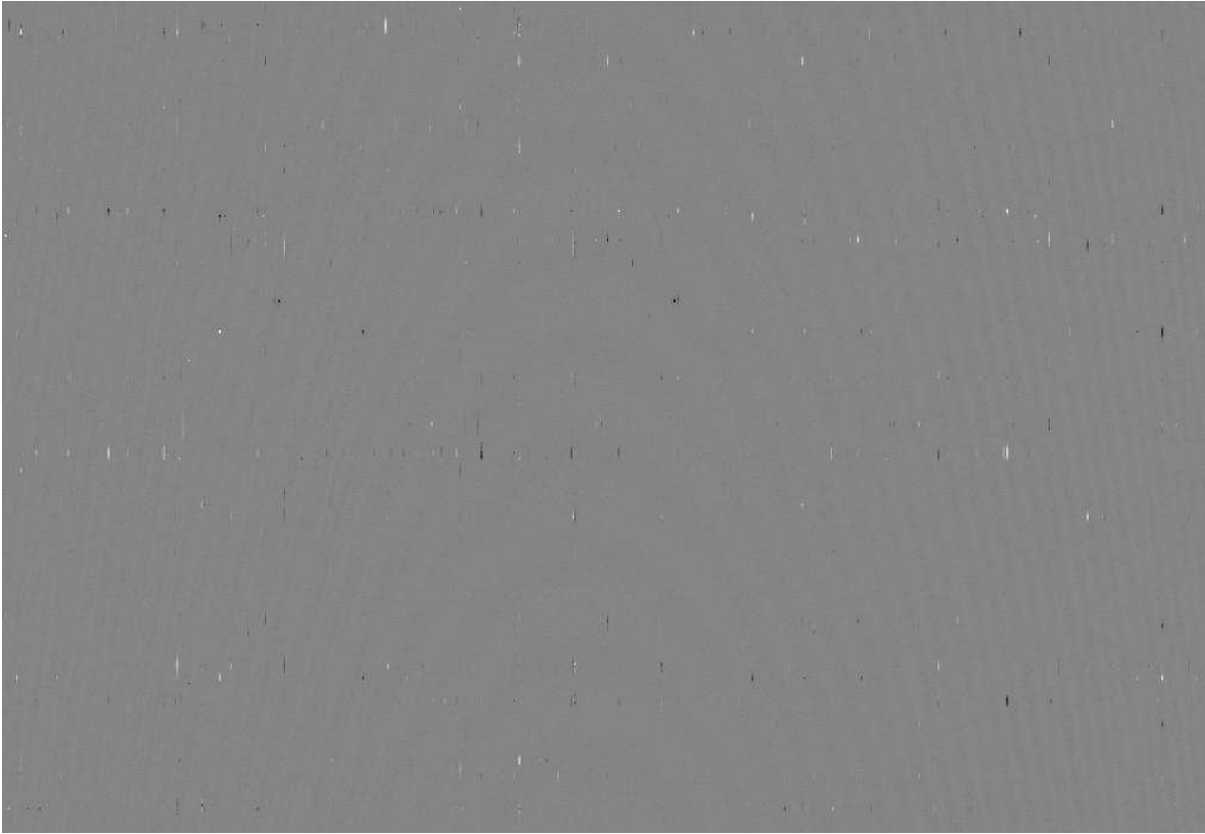


**Fig. 3** RFI reflections from meteor trails as seen in the raw baseline data. Time runs to the right, and a total of 4 hours are shown. Frequency increases upward, and we see the range 75-82 MHz. Only the real part of the correlation is shown, and the sign of the signal (black vs white) relates to the phase and direction of the source. Time resolution is 20 seconds.

Sporadically, when meteor trails allow propagation, RFI lines enter the spectrum. Most of these events are unresolved in time using our 20 second integrations, but there are a small number which extend over more than 2 bins. In these cases, the phases are always changing across our bins, as would be expected for a meteorite traveling more than our 10 arcminute fringe spacing in 20 seconds.

Eventually, these meteor trails can be tracked in real time in three dimensions. Multiple baselines allow a direct triangulation of the height. The velocity and direction of the trails can be reconstructed from the data, if one samples more finely after a trigger. It has been proposed (Sasa Nedeljkevic, private communications) that these meteor trails provide valuable information about the origin of the particles. PAST data will provide a large sample of data on the distribution of extrasolar grain, including detail on the trajectory and kinematics.

## 4.2 Galaxy

The sky brightness is dominated by synchrotron radiation from our Galaxy. The surface brightness near the NCP is  $T_{\text{gal}} = 280(150\text{MHz}/\nu)^{2.5}$ ,

Radiometric fluctuations due to this emission are the primary source of noise in our observations: this brightness determines the required integration time. Above the Galactic plane, the brightness is mostly smooth, and interferometry allows one to integrate stably down from the mean emission. The galactic synchrotron power spectrum above the galactic plane has been measured by Giardino et al. (2002) based on the 2.4 Ghz Parkes survey. Its structure drops in  $l^2 C_l \propto l^n$ , with a slope of about  $n \sim -1.5$  to  $l = 1000$ . Extrapolating a power law to the scales of interest, namely  $l \sim 3000$ , the galaxy has structure at the sub Kelvin level. This still potentially leaves the galaxy 2 orders of magnitude brighter in structure than the anticipated re-ionization signal. Fortunately, synchrotron emission has a mostly featureless frequency spectrum, which depends on the energy distribution of relativistic cosmic ray electrons. Zaldarriaga et al. (2003) have discussed some of the issues. We extend that discussion here. We are looking for spectral structure with  $\Delta\nu/\nu < 1\%$ , over which range one can model out the galaxy.

## 4.3 Point Sources

This same strategy will also work against the third class of foreground contaminants: point-like radio sources. These statistically dominate the power spectrum at  $l > 200$ . The bright point sources can be subtracted, and their contribution to the total power spectrum can be removed. These will also serve as the primary calibration source for the experiment. One constructs a three dimensional map, and adjusts the bright quasar continuum spectra as the reference for a featureless power law.

Several other sources of noise are present, which can be addressed by real-time data processing. These include sferics (atmospheric electric discharge like lightning) and meteor trails. Meteor trails generate higher density plasma which can reflect radio transmitters that are normally not visible. They last from small fractions of a second to many minutes, and must be detected in the data time stream and censored. It helps to have instantaneous location of point sources, which means covering two orthogonal axes with the baselines.

## 4.4 Ionospheric distortions

The ionosphere can generate phase delays and scintillations. The 6C survey, which observed at 150 MHz, reported 5 degree phase changes on km length baselines. These can either be calibrated and corrected using foreground sources, or ignored in a time average.

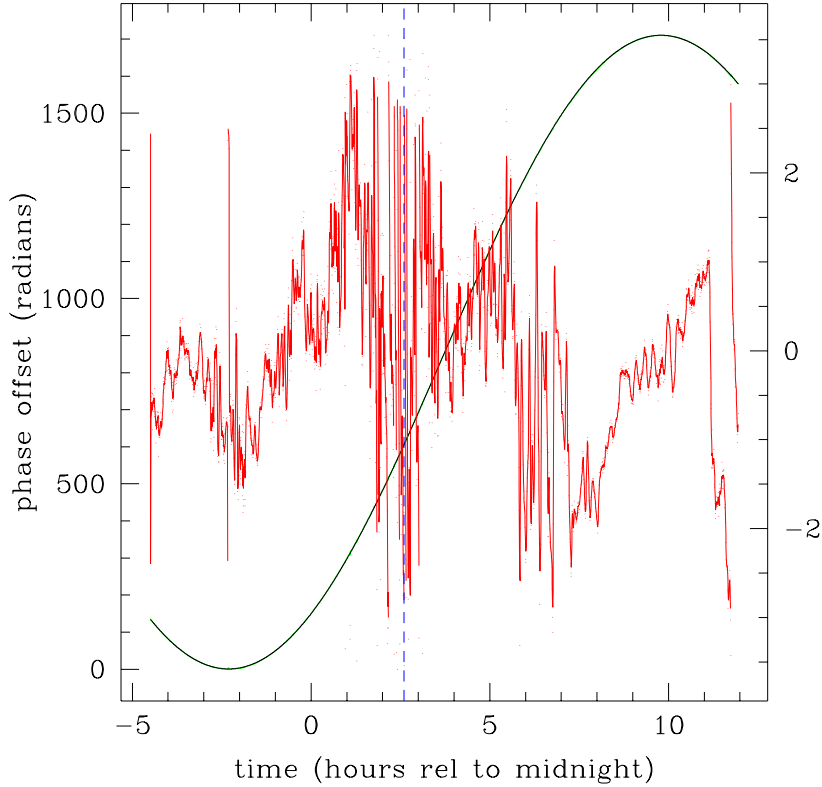


**Fig. 4** Phase delay of Cass A taken on a 1088m baseline on March 4, 2004. The horizontal axis is the time in hours. The smooth sinusoidal curve is the phase delay between the two baselines. The residual points with the magnitude scale on the right is the phase difference between the best fit sine wave. The solid jagged line is a 4 point boxcar average, corresponding to a 100 second integration. We observe scintillations with characteristic periods of 20 minutes. The dashed vertical line is the meridian passage, when Cass A passes through a maximal air mass of 4.4.

On the March 4 test run, we observed the phase of Cass A as it circles the NCP. The result is shown in Figure 4. Usable data was obtained in the frequency range 62-88 MHz. We observe typical scintillations with periods of 20 minutes, except near the meridian crossing of Cass A. At that point, Cass A passes through the lowest point on the sky, at an elevation of 13 degrees, corresponding to an air mass of 4.4. This maximizes the impact of the ionosphere, and also increases the projected phase fringe rate by the air mass.

We find a characteristic wave length for the isoplanactic structure to be 20km. This is significantly larger than the size of the array, and we expect to be able to solve for the instantaneous phase delays for bright sources using all pairs simultaneously. The

angular scale of ionospheric structure would be 5 degrees, which is comparable to the primary beam width. If desired, one could build a model to compensate for ionospheric variations. There is also a degeneracy in our data between spatial and temporal structure in the ionosphere. It is in principle possible that the ionosphere is varying in time, which could contribute to the variations that we observe. But the fact that the variations increase with airmass suggests that spatial variations dominate. The apparent velocity of the source against the ionosphere is proportionate to airmass.

In practice, the ionospheric delays are small enough at the NCP that they can be ignored without significantly affecting the image quality. Only for bright sources at large air mass, such as Cass A, does one need to track and subtract.

We show an image constructed from the test run data in Figure 5. The gray scale image used the data from one baseline integrating over 14 hours. The maps were constructed using the optimal techniques adopted from the CMB community, which is described in further detail below. In the small angle approximation, this is analogous to the aperture synthesis dirty map. The actual map making procedure is described below, and includes several aberrations from small angle map making (Cornwell & Perley, 1992).

## 5 DESIGN

We consider a general layout of  $N_d$  antennae of effective aperture  $A_{\text{eff}}$ . The effective aperture will be modeled relative to a single dish in both beam size and geometric cross section. For a given angular resolution, we assume that the dishes are distributed as a sparse subsampling of a single dish filled aperture reference antenna with the corresponding sized primary beam.

Initially, the experiment will be sensitivity limited, so we consider deep observations focused on the celestial pole. Earth rotation fills in the  $u - v$  plane. With  $N_d$  elements, one obtains  $N_d(N_d - 1)/2$  instantaneous baselines. If one arranges them to cover all separation lengths, earth rotation will result in all angular configurations. Specifically, if one achieves spacings that are multiples of the effective aperture diameter, and fills all baselines once, one obtains a resulting map which is spherical in the  $u - v$  plane containing  $\pi N_d^2(N_d - 1)^2/4$  pixels. Expanding our current prototype hexagonal geometry (Figure 1) to  $n$  rings requires  $1 + 3n(n + 1)$  elements. For  $n = 6$ , we obtain a 127 element pod. For an element spacing of 1.75m, the pod has a width of 20m.

A regularly spaced pod has Bragg reflection patterns at various resonant angles across the sky. These sidelobes can be suppressed by a slight shuffling of spacings. Figure 6 shows an arrangement of the 127 elements in a pod which reduces the regular first order resonances. The resulting beam response is shown in figure 7.

The maximum size of the pods is determined by the need to achieve redundant spectral imaging. In order to overcome the bright foregrounds, we will always be differencing

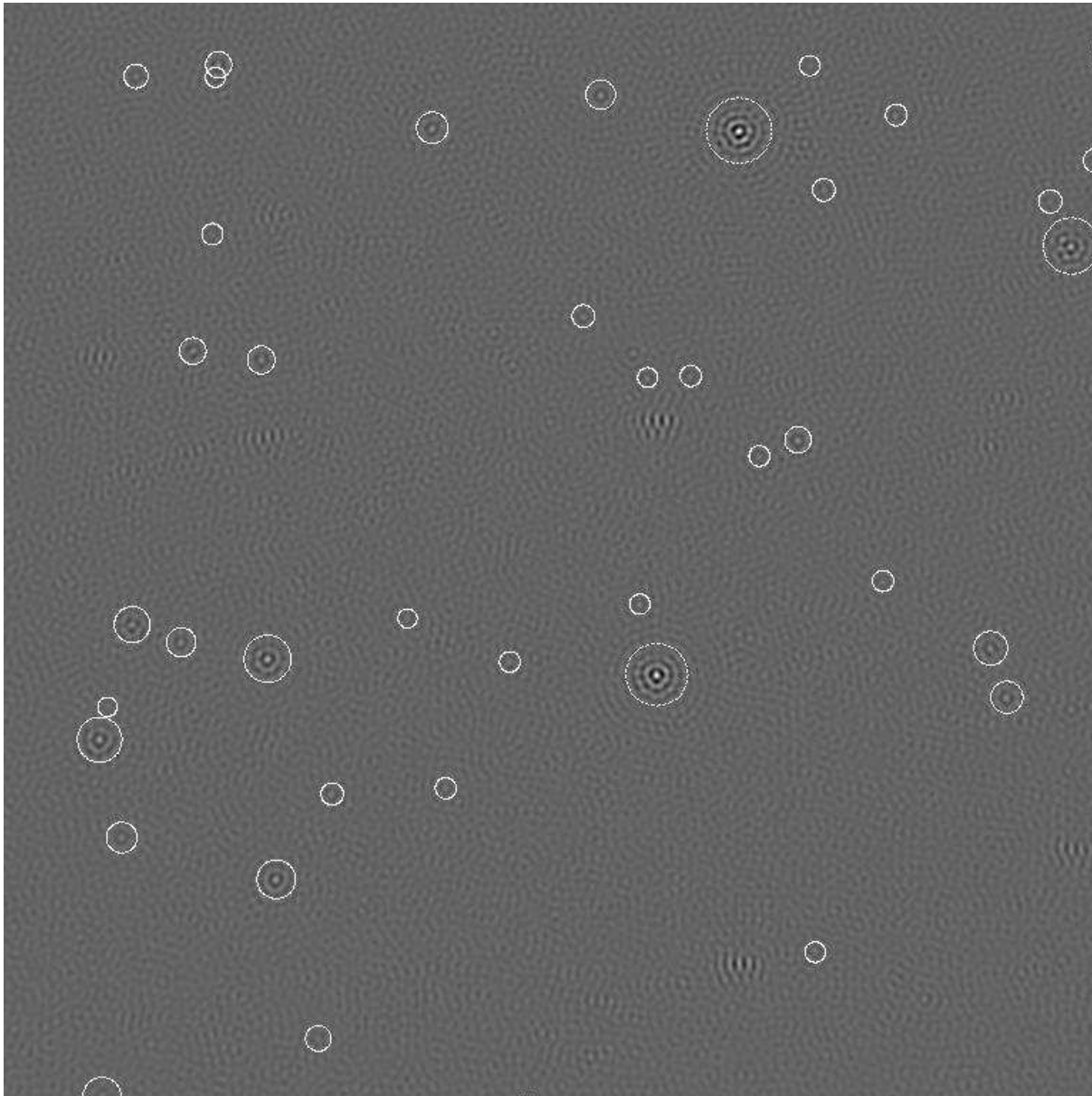


**Fig. 5** Image reconstructed using the 1088m east-west baseline. The displayed field of view is 24 degrees. Frequency range is 62-88 MHz. Overlaid on the gray scale map from the PAST prototype are 8C sources with flux greater than 10 Jansky shown as circles. The area of each circle is proportionate to the 8C flux. The adjoint map making procedure brings objects into focus anywhere on the sky.

maps at different frequencies. In order to do the differencing at fixed angular scale, the baselines to be differenced must be of different physical scale. The closer in frequency one applies the differencing, the less susceptible one is to changes in spectral structure of the foregrounds. There is a lower limit, however. The frequency difference must be

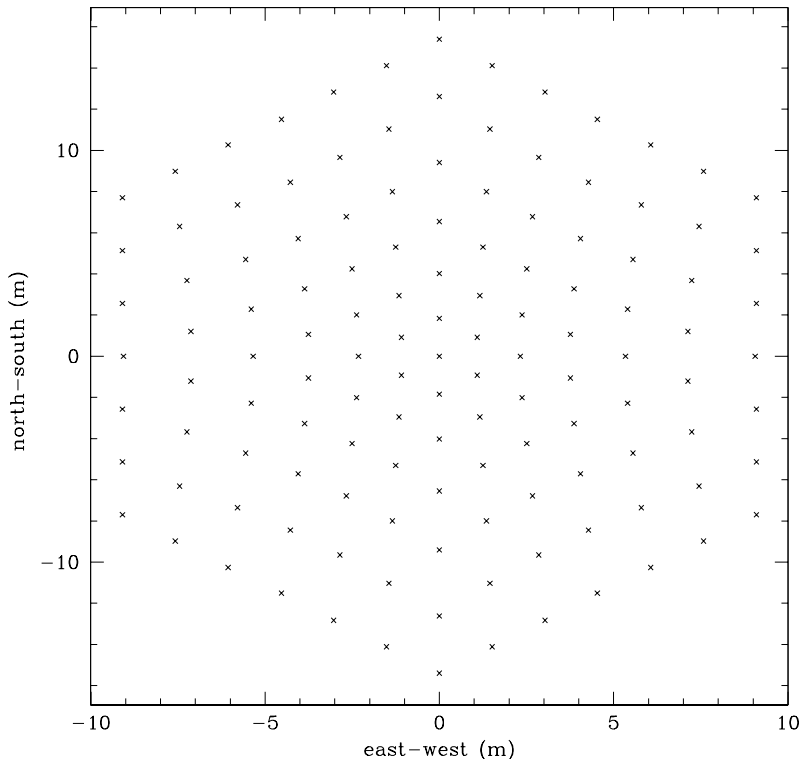


**Fig. 6** Rearranged elements with a 127 element pod to reduce the strength of Bragg sidelobes.

larger than the structures that we are searching for. This limits the largest possible frequency structures that one can image. We anticipate structures up to 40 Mpc in diameter (Wyithe & Loeb, 2004), which is 2% in frequency. In order for the baselines to be distinct in the  $u-v$  maps, the pods should be no larger than 30m for a 1.5km baseline.

With 40 elements, one obtains about 780 baselines. One expects about 10 redundant baselines per non-redundant configuration if they cover a 2km area and recover all the frequency information of a filled aperture of 2km diameter.

Direct permutation layouts show that in one dimension, one can come to within 20% of a perfect non-redundant compact configuration. This means that 20% of baselines are either redundant, or cover non-contiguous parts of the  $u-v$  plane. Using two sets of 10 pods over 67 pod diameters (which we call 'pod units') covers all baselines configuration out to 36 pod units, including all correlations across and within each size class. We then duplicate this configuration separated by 73 pod units, which covers all baselines up to 109 pod units continuously, shown in Figure 9. The longest baseline is 139 pod units.

Actual sensitivities depend on configuration, noise and angular scale. An approximate non-redundant linear array of 10 elements from an exhaustive search shown in figure 8.



**Fig. 7** Polar projection of beam pattern for the array populated with isotropic receivers. This shows the worst case side lobes, which occurs at the shortest wavelength, i.e. 200 Mhz. A spacing of 1.75m projected on the NCP was used. The small residual side lobes are further suppressed by 20 dB due to the primary beam of each log periodic. The horizontal scale is 180 degrees, the vertical scale is 120 degrees. The primary beam is actually round when viewed from the NCP.

The actual beam pattern of a rotation averaged non-redundant array is similar to a filled aperture diameter corresponding to half the array size.

To estimate sensitivities, we first estimate the sensitivity of a single dish on a given length scale, and then scale by the dilution factor of the array. We will use 150 MHz as the central reference frequency. From the Haslam (Haslam et al., 1981) maps, we find the mean temperature in a 10 degree beam on the north celestial pole to be 25K. The spectral index near the NCP is 2.5 (see below). We expect a foreground noise temperature of  $280(150\text{MHz}/\nu)^{2.5}\text{K}$ . We budget a further 100K for receiver and system noise. The galaxy is the dominant noise source in the frequencies of interest, 50-200 MHz. The NCP is less than a factor of two warmer than the coldest spots on the sky.

A reasonable estimate for the large scale strong features during re-ionization might be 10 comoving Mpc, which is 5 arc minutes. Some estimates are even larger than this

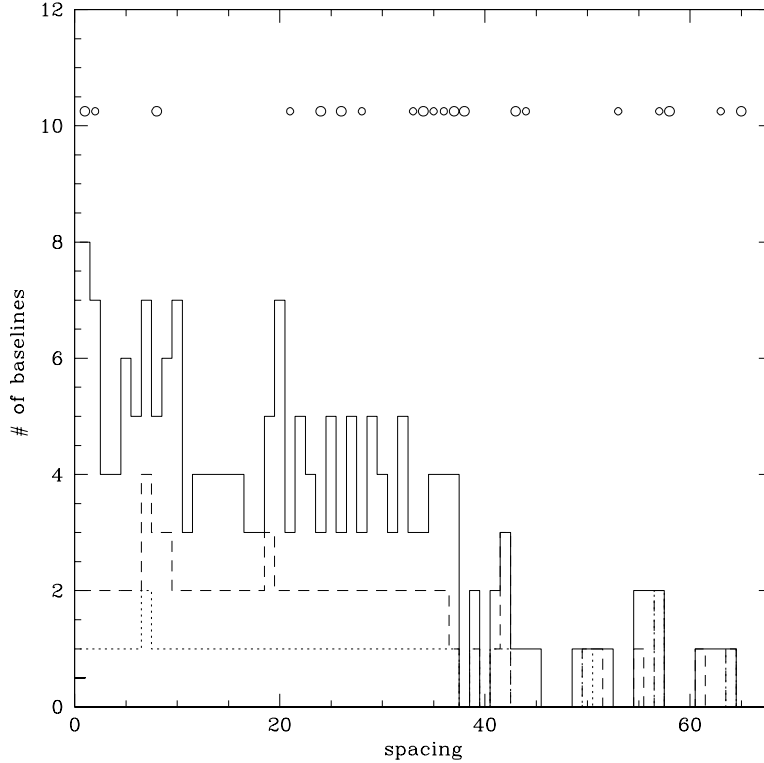


**Fig. 8** Minimum redundancy configuration for two sets of 10 elements. The combinatorial upper limit is 45 baselines covering every spacing from 1 to 45 exactly once. This actual configuration covers all spacings up to 36 at least once, and is from an exhaustive search on all permutations. The top row of circles denotes the location of pods, with large circles representing the initial pods and vice versa. The histograms represent the cumulative number of initial, secondary, and total baselines.

value (Barkana & Loeb, 2003). The observed quasars at  $z=6.28$  and  $z=6.41$  appear to have Stromgren spheres with diameters of greater than 40 comoving Mpc (Wyithe & Loeb, 2004).

Aiming at  $10 h^{-1}$  Mpc corresponds to an aperture scale of 1.4 km. One would expect features to have comparable sizes radially. The radial distance is  $58 h^{-1}$  km/s/Mpc (comoving) at  $z = 9$  for an  $\Omega_0 = 0.3$   $\Lambda$ -CDM cosmology, so these 10 Mpc correspond to 300 kHz bandwidth. The sensitivity for a filled dish of diameter  $d_f = 1.4(5'/\theta)$  km is

$$\Delta T = 2.5 \left( \frac{150 \text{ MHz}}{\nu} \right)^{2.5} (10 h^{-1} \text{ Mpc } L)^{-1/2} \left( \frac{24h}{t} \right)^{1/2} \text{ mK.} \quad (1)$$

The expected temperature change is 25 mK for an isolated Stromgren sphere, so one achieves a S/N of order 10 in one day after a full rotation of baselines. The time increases as the array dilution factor, so if one wishes a  $1 - \sigma$  map in four months, one can reduce

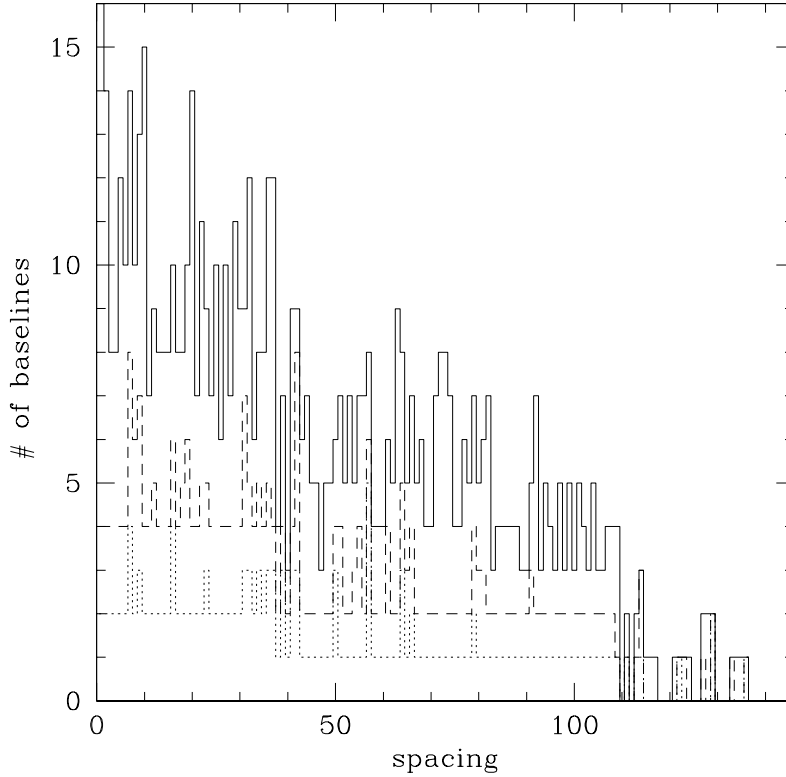


**Fig. 9** Baseline coverage with two sets of 10 pods offset by 73 pod units.

the collecting area from  $1.5 \text{ km}^2$  to  $1/100$ th that value. If each basic antenna has an area of  $1.5 \text{ m}^2$  (a gain of 7 dbi), this is achieved with the 80 pod configuration of approximately 10,000 antennae.

With a fixed number of antenna spread out over a 2km baseline, the sensitivity increases rapidly for larger ionizing structures. For the array, we expect radiometric uncertainty

$$\Delta T = 22 \left( \frac{150 \text{ MHz}}{\nu} \right)^{2.5} (20h^{-1} \text{ Mpc} L)^{-2.5} \left( \frac{24h}{t} \right)^{1/2} \text{ mK}. \quad (2)$$

A week long observation should identify all ionized structures larger than  $20 \frac{1+z}{10} \text{ Mpc}$  at more than three sigma. This sensitivity is well matched to the inferred large ionization spheres around SDSS quasars, which are twice as big and should be well resolved.

One can also aim for a statistical detection of the power spectrum. If reionization occurs over the redshift range of  $\Delta z \sim 2$ , we have 100 Stromgren spheres of  $10h^{-1} \text{ Mpc}$  diameter radially. If we use a pod beam of  $10^\circ$ , we expect about a million three dimensional resolution cells of  $10h^{-1} \text{ Mpc}$ . One can measure the average RMS variation between cells 30 times more sensitively than the actual value of each cell. With a total

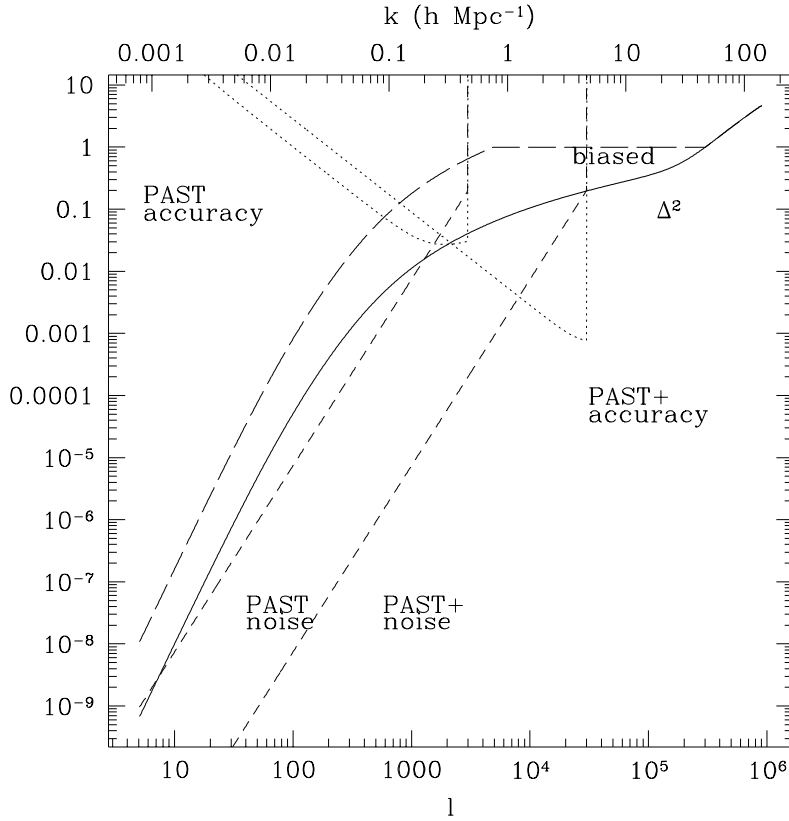


**Fig. 10** Matter power spectrum measurement. Solid line: the matter power spectrum at  $z = 9$ . One expects the 21cm emission to trace the total mass. Long-dashed line: power spectrum of patchy re-ionization with a bias  $b = 4$ . Short-dashed lines: noise level expected for PAST and second generation PAST+. Dotted line: fractional accuracy of power spectrum measurement per logarithmic  $l$  bin.

collection area of  $15000 \text{ m}^2$ , one can measure a  $10\text{mK}$  RMS power spectrum to  $1000 \sigma$  in 100 days. This is quantified in Figure 10.

To summarize: 50 pods are needed to cover the  $u - v$  plane completely. A two dimensional structure is important to localize emission. At the same time, one needs many baselines with similar length to be parallel to each other, so one can do simultaneous beam frequency correction. A T-shaped array with 50 elements on each axis would satisfy such requirements. However, an array with fewer elements may suffice if foreground removal can be accomplished using incomplete uv coverage.

## 6 FOREGROUNDS

### 6.1 Redundancy

Each pod is a large array of phased antennae. The maps are made from baselines, and the sensitive measurements rely on a careful comparison of spectral and spatial information. This comparison will necessarily require comparing differing baselines. For example, a 1 km baseline at 150 MHz needs to be compared to a 1.1km baseline at 136 MHz to achieve the same spatial scale. While the baselines can be matched, the primary beams may still differ. This can be corrected for in the processing. To compare two maps with different beams, one convolves the first map with the second map's beam and vice versa, so they have a common beam. One strategy to cross check for beam systematics is to use two sets of pods, possibly scaled by a small geometric factor. This also makes a natural deployment sequence, and we will discuss two generations of pods, either one of which can make a complete image of the sky. Individual elements within a pod may fail. It is thus clearly important to be able to map the primary beam to high accuracy. Fortunately, the beams can be mutually calibrated. Each baseline corresponds to factor of two range in angular scale over the frequency band, which allows the construction of a mostly complete u-v map from one baseline alone, as was done for Figure 5 using the prototype test data. The grid of point sources as shown in figure 11 is mapped by each baseline. The relative brightness of the point sources measures the shape of the primary beam of the product of the pods. This allows one to solve for the primary beams, given the redundancy in the number of baselines.

For example, if one element in one pod failed, one would find that all baselines which involve this element would have a changed primary beam. The primary beam is in turn a Fourier transform of the aperture, so one can directly identify which element has failed.

### 6.2 Radio Sources

The 6C survey of radio sources is based on an analogous concept of a linear array of antennae at 151 MHz, which is in the middle of the range of interest for PAST. We can use it as a good guide to the expected level of radio contamination at our frequencies of interest. Figure 11 shows the location of radio sources near the north celestial pole. The brightest source is 42 Jansky, and the source counts are consistent with  $d \log N/d \log S \sim -2.5$ . The total flux is dominated by the collective faint sources. The cutoff in this integral is not well known. At 150 MHz, the conversion from flux to surface brightness is 1 Jy/sq degree=3.7K. For a primary beam of 10 degrees, which corresponds to the central part of the map in Figure 11, the total brightness contribution from resolved point sources in the 6C survey would be 13K. This is clearly a lower bound on the total unresolved extragalactic background, which will contribute to Poisson noise. Extrapolating deep

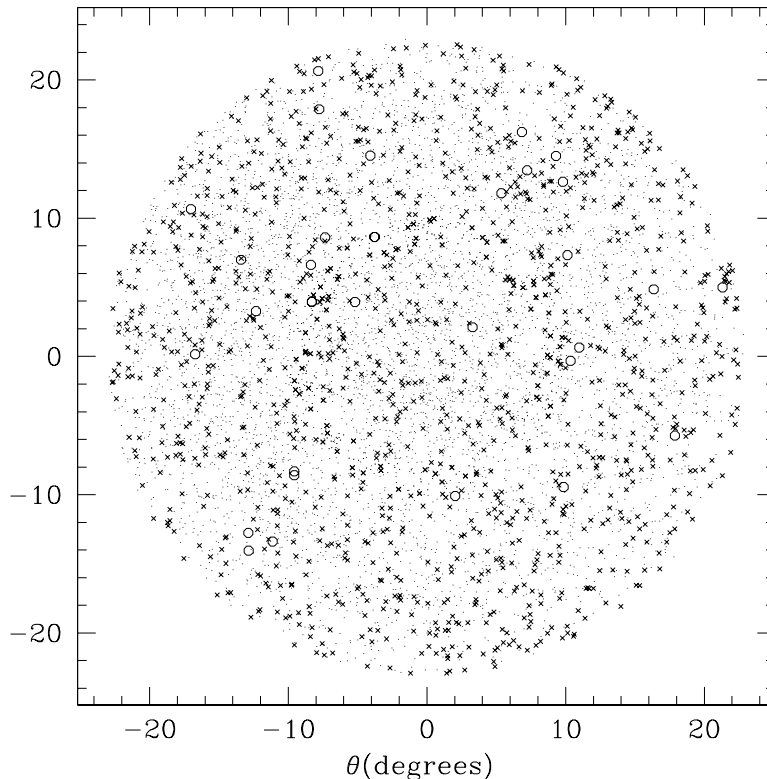


**Fig. 11** Distribution of 6C sources at 151 MHz around the NCP. Circles are fluxes greater than 10 Jy, crosses between 1 and 10 Jy, and dots less than 1 Jy. The brightest source is 32 Jy.

surveys to 6mJy at 610 MHz (Willis et al., 1977) results in a 48K background from point sources. Those counts appear convergent, and extrapolating to fainter fluxes only adds 3K to the background. The cosmic microwave background adds another 2.7K.

At the confusion limit, we resolve sources down to 5', which should resolve all sources down to 50 mJy. While the total flux is dominated by faint sources, the fluctuations are dominated by bright ones. The residual fluctuations on 5 arcminute synthesized beams would then be of order 25 K, which is expected to be larger than the fluctuation in galactic structure. The same procedure to remove the galaxy should also apply to radio sources. One could also add longer baselines to further deconfuse the point source background.

### 6.3 Galactic Emission

The absolute temperature of the galaxy in the NCP region over the VHF band has been well characterized over the last century. Turtle & Baldwin (1962) measured at 178 MHz, and find a surface brightness of 175K at NCP. They report a calibration error of 5% and a zero point error of less than 10K. In the 408 Haslam maps, the same point is reported

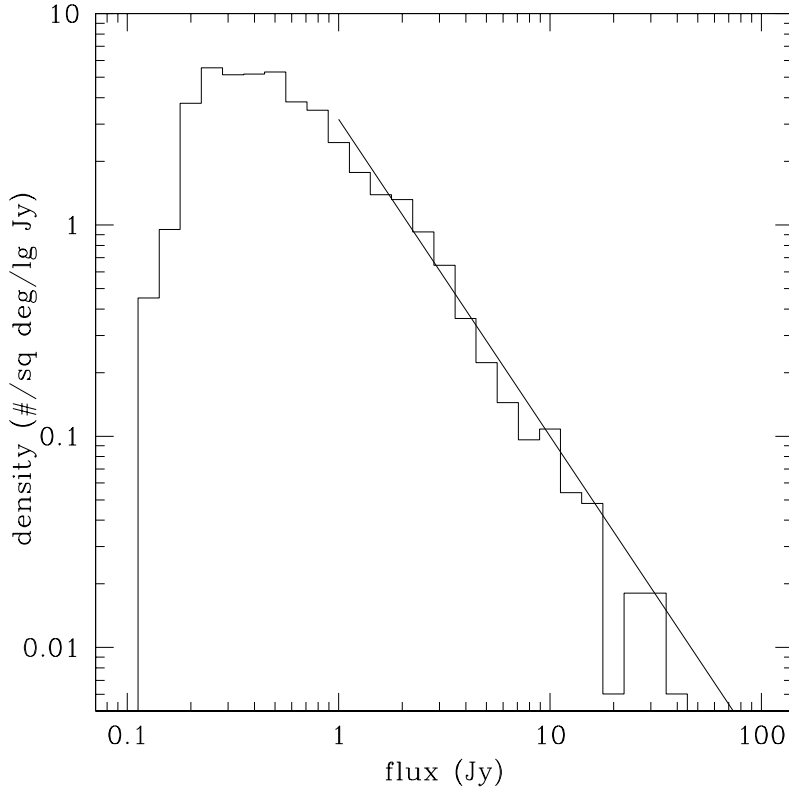


**Fig. 12** Flux counts of 6C sources at 151 MHz. The line segment represents  $N(> S) \propto S^{-1.5}$ . The total flux is dominated by the unresolved faint end, while the fluctuations are dominated by the brightest.

at 25K. Haslam reports a less than 10% calibration uncertainty, and a zero point error of 3K. These numbers result in a spectral index  $T \propto \nu^\beta$  with  $-2.7 < \beta < -1.9$ . This is significantly shallower than the values of  $\beta = -3$  reported by WMAP (Bennett et al., 2003) and Parkes (Giardino et al., 2002). The low frequency synthesis of Lawson et al. (1987) report  $\beta = -2.5$  at the NCP. We shall adopt that value for the frequency range of PAST. The total temperature budget scaled from 178 MHz is then 280K at 150 MHz, which is dominated by the galaxy.

## 7 MAP MAKING

Observing the North Celestial Pole is a form of drift scanning. Drift scan interferometry places unique requirements on the construction of maps. The CMB community has studied the general theory of map making (Tegmark, 1997). With PAST we will have quite uniform uv coverage, and we are searching for extended objects across the entire field. The style of our observations and analysis is closer to CMB observations than to typical radio observations, which may have limited uv coverage, and anisotropic beams.

For us, each baseline can be thought of as generalized pixels with some noise and beam. We will simplify and apply CMB mapping theory to the interferometric construction of EoR maps.

Each baseline can be considered a single pixel detector which drift scans the sky. The real and imaginary parts of the fringe can be used to construct separate maps. We can think of the visibilities for each baseline and each frequency to be a set of generalized pixels. We denote them  $\mathbf{v}$ . Their noise is uncorrelated, so the noise covariance matrix  $\mathbf{N} \equiv \langle \mathbf{v}\mathbf{v}^t \rangle$  is diagonal. Each of these generalized pixels samples the sky through the visibility beam. We can think of this as a linear map  $\mathbf{v} = \mathbf{P}\Delta$ , where  $\Delta$  is the set of temperatures at each point on the sky. The optimal map reconstruction is then  $\tilde{\Delta} = \mathbf{P}^\dagger \mathbf{N}^{-1} \mathbf{v}$ . This map is the true map convolved by the synthesized beam  $\mathbf{B} \equiv \mathbf{P}^\dagger \mathbf{N}^{-1} \mathbf{P}$  so  $\tilde{\Delta} = \mathbf{B}\Delta$ . We see that the intrinsic computational cost for the most general algorithm scales as the square of the number of pixels.

The remainder of this section discusses how to implement this procedure at a lower computational cost, and show some implementations of algorithms such as CLEAN. In the subsequent analysis, we treat each pod as a uniformly filled dish.

Let us first consider the real space window of a baseline. We approximate each pod as a circular filled aperture. The real component of the fringe with baseline along the  $x$ -axis results in a window

$$W_R(x, y) = \cos(2\pi n u_0 x) \frac{J_1(\sqrt{x^2 + y^2} \pi u_0)^2}{(x^2 + y^2) \pi^2 u_0^2} \quad (3)$$

in terms of the Bessel function  $J_1$  with the imaginary component resulting in

$$W_I(x, y) = \sin(2\pi n u_0 x) \frac{J_1(\sqrt{x^2 + y^2} \pi u_0)^2}{(x^2 + y^2) \pi^2 u_0^2}. \quad (4)$$

$n = 1$  corresponds to the shortest spacing, and larger spacings increase  $n$  proportionately. Figure 13 shows the of the window function in real space. We note that using the short baselines, the full-width at half-max (FWHM) of the real component of the beam is 0.41 of the FWHM of a single aperture with the same diameter. The FWHM is measured as the separation along the baseline vector at which the real component beam drops from its peak halfway to its global minimum.

We call the optimal weighted maps *raw map*, and proceed to fancier procedures including wiener filtering and CLEAN.

## 7.1 Raw Maps

Let us normalize each base line to have unit noise per pixel. Then for a given baseline window (of which there are two per baseline, one real and one imaginary) at an hour angle  $\phi$ , the visibility map is given as  $L_i(\phi) = \int d^3\mathbf{x} W_i(\mathbf{x}, \phi) S(\mathbf{x}) + N$ , where  $S$  is the true sky map,  $W_i$  is the  $i$ -th window function normalized in such a way to give unit

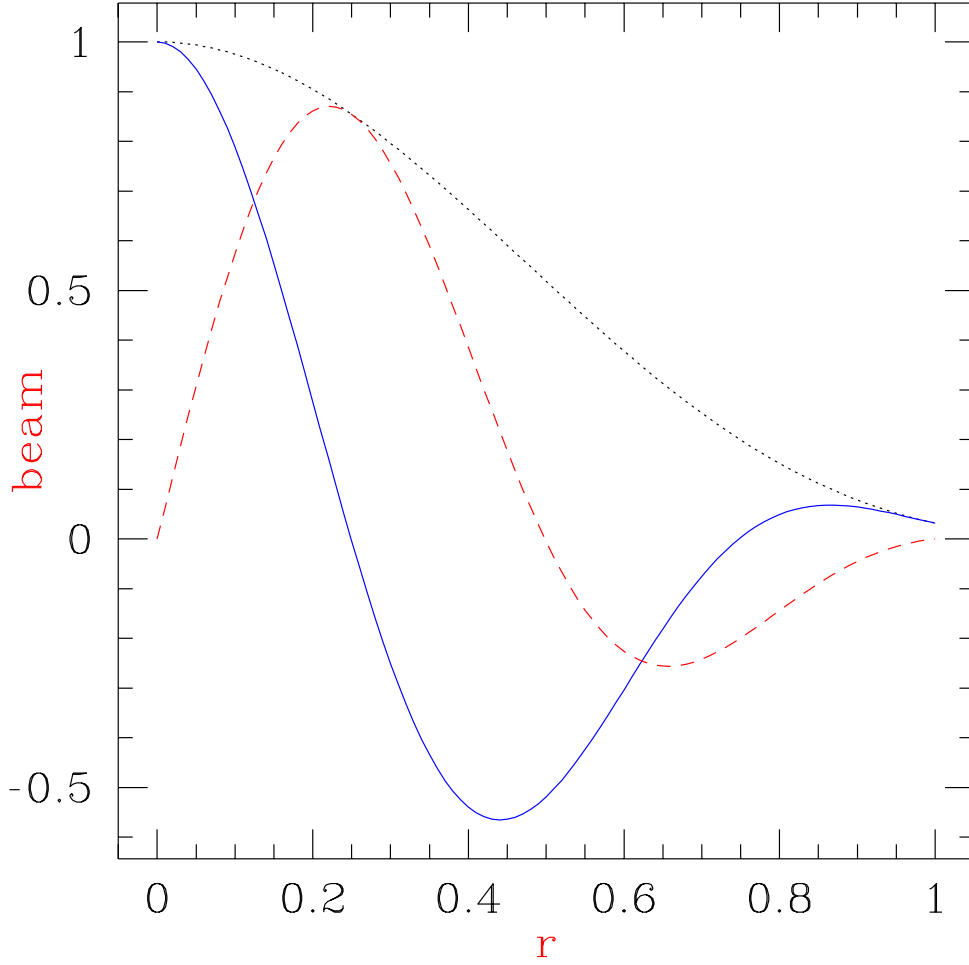


**Fig. 13** Real space beam pattern of the correlation fringe of a close packed baseline. Scale is in units of primary beam FWHM. The solid line is the beam from the real component of the correlation fringe along the baseline vector. The dashed line is the imaginary component, and the dotted line the primary beam. Perpendicular to the baseline the window is determined by the primary beam.

noise variance in the map, and  $N$  is white noise with unit variance per pixel. The raw map is then

$$\tilde{S}(\mathbf{x}) = \sum_i \int W_i(\mathbf{x}, \phi) L_i(\phi) d\phi \quad (5)$$

We then define the *raw beam* to be

$$W_R(\mathbf{u}) = \sum_i W_i(\mathbf{u})^2. \quad (6)$$

This raw beam transformed back to angular space is shown in Figure 14. We will subtract the mean signal from each scan since that contains ground, cross talk and other stationary contaminants. This effectively slightly modifies the window functions.

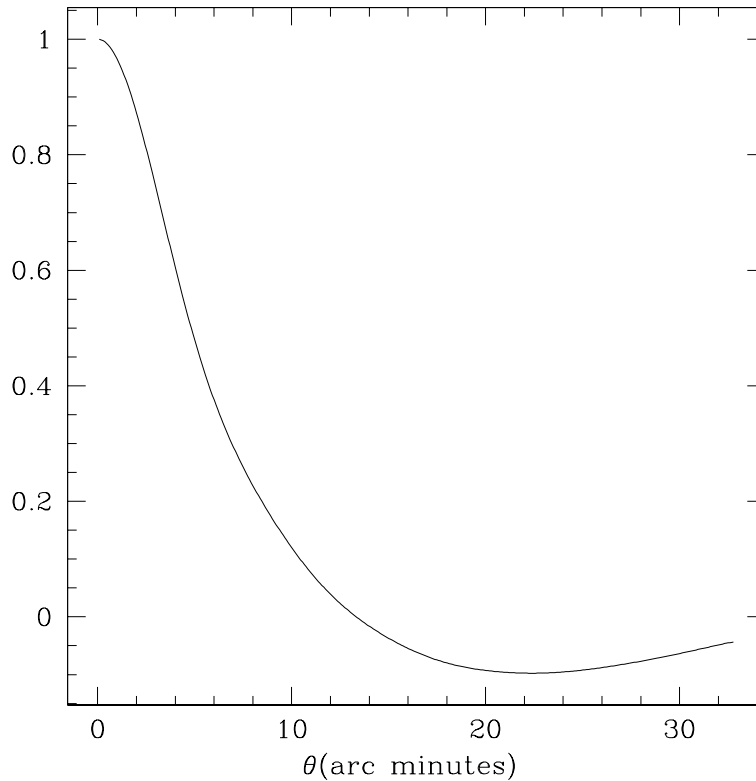


**Fig. 14** Raw beam of PAST. This raw beam is the autoconvolution of what is commonly called the resolution beam.

## 7.2 Co-linear Base Line Maps

The fractional bandwidth of PAST is large. Most sources are synchrotron emitters with similar spectral index. We can then treat the different frequencies as different effective baseline lengths. The fixed baseline on earth measured in wavenumbers is a function of frequency, and we can get a factor of two or more in scales from one baseline alone. The prototype map in Figure 5 was made from a single baseline. Instantaneously one obtains a one dimensional map, as a function of wavelength. Earth rotation maps this one baseline onto all angles, resulting in a two dimensional map. In the full array, one will be able to simultaneously construct a set of co-linear baselines at each frequency independently, resulting in an instantaneously two dimensional map (spatial and frequency), which earth rotation will fill in as the final full three dimensional map.

The baseline visibility at a given frequency sees the sky multiplied by the primary beam, projected along the baseline, and Fourier transformed. The adjoint operation is the inverse Fourier transform, projection onto the sky, and weighting by the beam. The projection is a scatter operation, which we can juxtaposition into a gather: each pixel on the sky samples the Fourier transform of a baseline at each position angle.

### 7.3 Cleaned Maps

Densely sampled drift scanning differs fundamentally from image reconstruction in traditional radio interferometry. Typically, the  $u$ - $v$  plane is sparsely sampled, and images can never be fully reconstructed even in principle. Statistical techniques, such as Bayesian priors or maximum entropy methods are employed to fill in the missing information.

For fully sampled arrays like PAST, there are no gaps on the  $u$ - $v$  plane, and the synthesized beam is very “clean”, i.e. does not possess significant side lobes, as can be seen in figure 14. For non-overlapping point sources, the raw maps are the likelihood function. Peaks in the raw maps can then be identified as point sources. The signal-to-noise is easily known, and can be read off from the diagonal elements of the noise variance matrix  $\langle \tilde{\Delta} \tilde{\Delta}^t \rangle = \mathbf{P}^\dagger \mathbf{N}^{-1} \mathbf{P}$ , which is linearly proportional to the diagonal elements of the beam matrix  $\mathbf{B}$ .

But we may still be concerned about point sources that are “noise” in the quest for intrinsic 21cm fluctuations. It is desirable to be model point sources to as low a flux limit and as high an accuracy as possible.

### 7.4 Homogeneity of an east-west array

It has long been known that a pure east-west array does not have most of the issues that we have discussed above. This is because fringe pattern of an E-W baseline is symmetric about a N-S line on the sky. A N-S baseline is inclined with respect to the line of sight (except for an array site at a Pole of the Earth). Fringes in the Northern half of the fringe pattern are spaced closer together than those in the Southern half.

Many of the early radio astronomy arrays were laid out along an east-west direction for this reason. For a co-linear array, one can lay the baselines into a  $u$ - $v$  plane, and apply a fast Fourier transform. The real space map is then the celestial sphere projected down the NCP, and the interferometric beam is homogeneous. Our prototype pods were 11 degrees off from the perpendicular line to the NCP, and the non-flat sky problems arose even 10 degrees from the NCP.

An east-west array has the benefit that the far side lobes of bright sources will be easier to understand. Also, being co-linear, the anisotropies in the primary beam always have the same alignment relative to the fringes. Searching for small spectral structure against bright foregrounds, this allows for a cleaner subtraction of neighboring spectral maps. As the earth rotates, bright sources can cross the limb of the Earth, the ionosphere can change in absorption or refraction, man-made EMI can change, and the instrumental offsets can drift. If all baselines lengths are observed at the same time in the same position angle on the sky, these effects all cancel when constructing difference maps at neighboring frequencies.

## 8 GLOBAL ALL-SKY SPECTRA

In addition to imaging the ionization structure, one could use PAST as a tool to measure the absolute spectrum of the sky. The global reionization of the universe imprints a 20 mK feature on the global diffuse spectrum. An array of 100 elements each taking independent spectra would achieve a sensitivity of 20 mK over a 1 MHz bandwidth at 150 MHz in less than two minutes. If reionization completed rapidly, as is generally believed, the small global signal can be measured with PAST.

## 9 CONCLUSIONS

We have reviewed the current state of our understanding of re-ionization, which points to a complex history with ionization structure likely to exist on a range on length and time scales. The ionized regions are visible as holes in emission against the neutral background, which can be imaged interferometrically.

Estimates of the reionization scenarios show that the structures are at frequencies, angular scales and flux levels that are accessible to existing radio astronomy facilities. The only obstacle is the serious level of radio interference on the VHF band, which includes commercial TV and FM radio.

We have presented estimates of the strength of the signal for currently best guess models of the Epoch-of-Reionization scenarios. The PAST experiment should have sufficient sensitivity to image the larger structures with diameters of  $20h^{-1}$  Mpc, and one can obtain 3-D maps with high signal-to-noise over a period of weeks. Smaller scales can be probed statistically, in analogy with the current weak lensing and CMB surveys. The PAST maps will have up to 2.5 arc minute resolution with a field of view of 5 degrees, and at least 10,000 resolution in redshift.

We have investigated the effects of various sources of noise and foregrounds. The dominant noise source is the galaxy, which makes the remaining instrumental noise characteristics easy to control. Other sources, including man-made interference, meteor trail reflections, extra-galactic radio sources, and others, have been studied in the PAST prototype. All celestial sources have featureless continuum spectra, while the reionization sources have spectral structure. All prototype data indicates that the sensitivities should be realistically achievable. We have addressed several processing challenges, and demonstrated efficient map construction on the curved sky.

**Acknowledgements** This work was funded by the Natural Science Foundation of China (NSFC).

## References

Barkana R., Loeb A., 2003, ArXiv Astrophysics e-prints, pp 10338+

- Bennett C. L., Hill R. S., Hinshaw G., Nolte M. R., Odegard N., Page L., Spergel D. N., Weiland J. L., Wright E. L., Halpern M., Jarosik N., Kogut A., Limon M., Meyer S. S., Tucker G. S., Wollack E., 2003, *ApJS*, 148, 97
- Briggs F. H., Bell J. F., Kesteven M. J., 2000, *AJ*, 120, 3351
- Cen R., 2003, *ApJ*, 591, 12
- Cornwell T. J., Perley R. A., 1992, *A&A*, 261, 353
- Furlanetto S. R., Sokasian A., Hernquist L., 2004, *MNRAS*, 347, 187
- Giardino G., Banday A. J., Górski K. M., Bennett K., Jonas J. L., Tauber J., 2002, *A&A*, 387, 82
- Haslam C. G. T., Klein U., Salter C. J., Stoffel H., Wilson W. E., Cleary M. N., Cooke D. J., Thomasson P., 1981, *A&A*, 100, 209
- Iliev I. T., Scannapieco E., Martel H., Shapiro P. R., 2003, *MNRAS*, 341, 81
- Kogut A., Spergel D. N., Barnes C., Bennett C. L., Halpern M., Hinshaw G., Jarosik N., Limon M., Meyer S. S., Page L., Tucker G. S., Wollack E., Wright E. L., 2003, *ApJS*, 148, 161
- Lawson K. D., Mayer C. J., Osborne J. L., Parkinson M. L., 1987, *MNRAS*, 225, 307
- Madau P., Meiksin A., Rees M. J., 1997, *ApJ*, 475, 429
- Pelló R., Schaerer D., Richard J., Le Borgne J.-F., Kneib J.-P., 2004, *A&A*, 416, L35
- Pen U.-L., 2004, *New Astronomy*, 9, 417
- Shaver P. A., Windhorst R. A., Madau P., de Bruyn A. G., 1999, *A&A*, 345, 380
- Tegmark M., 1997, *Phys. Rev. D*, 56, 4514
- Turtle A. J., Baldwin J. E., 1962, *MNRAS*, 124, 459
- White R. L., Becker R. H., Fan X., Strauss M. A., 2003, *AJ*, 126, 1
- Willis A. G., Oosterbaan C. E., Lepoole R. S., de Ruiter H. R., Strom R. G., Valentijn E. A., Katgert P., Katgert-Merkelijn J. K., 1977, in *IAU Symp. 74: Radio Astronomy and Cosmology Westerbork Surveys of Radio Sources at 610 and 1415 MHz*. pp 39–+
- Wyithe S., Loeb A., 2004, *ArXiv Astrophysics e-prints*, pp 01188+
- Zaldarriaga m., Furlanetto S., Hernquist L., 2003, *ArXiv Astrophysics e-prints*, pp 11514+